Macropinocytosis-mediated membrane recycling drives neural crest migration by delivering F-actin to the lamellipodium

Yuwei Li[a], Walter G. Gonzalez[a], Andrey Andreev[a], Weiyi Tang[a], Shashank Gandhi[a], Alexandre Cunha[b,c], David Prober[a], Carlos Lois[a], and Marianne E. Bronner[a,1]

[a]Division of Biology and Biological Engineering, California Institute of Technology, Pasadena, CA 91125; [b]Center for Advanced Methods in Biological Image Analysis, Beckman Institute, California Institute of Technology, Pasadena, CA 91125; and [c]Center for Data-Driven Discovery, California Institute of Technology, Pasadena, CA 91125

Contributed by Marianne E. Bronner, September 22, 2020 (sent for review June 8, 2020; reviewed by Angela Nieto and Tatjana Piotrowski)

Individual cell migration requires front-to-back polarity manifested by lamellipodial extension. At present, it remains debated whether and how membrane motility mediates this cell morphological change. To gain insights into these processes, we perform live imaging and molecular perturbation of migrating chick neural crest cells in vivo. Our results reveal an endocytic loop formed by circular membrane flow and anterograde movement of lipid vesicles, resulting in cell polarization and locomotion. Rather than clathrin-mediated endocytosis, macropinosomes encapsulate F-actin in the cell body, forming vesicles that translocate via microtubules to deliver actin to the anterior. In addition to previously proposed local conversion of actin monomers to polymers, we demonstrate a surprising role for shuttling of F-actin across cells for lamellipodial expansion. Thus, the membrane and cytoskeleton act in concert in distinct subcellular compartments to drive forward cell migration.

membrane recycling | actin turnover | macropinocytosis | cell migration | neural crests

Cell migration is central to embryogenesis, organogenesis, and cancer metastasis (1, 2). Individual migrating cells rapidly change their shape via cycles of protrusion and retraction (3, 4), raising the question of how a cell distributes its limited amount of membrane to maintain polarized morphology without affecting membrane integrity. Early studies, based on observing the movement of cross-linked antigen on the cell surface, proposed a "membrane flow" model to explain the role of membrane recycling during cell locomotion (5–8). This two-dimensional (2D) model posits that cells undergo clathrin-mediated endocytosis in the rear of the cell, which generates anterograde flow of lipid vesicles and retrograde flow of membrane (Fig. 1*A*). Such a retrograde membrane flow could enable membrane proteins to generate traction forces against the extracellular matrix (ECM) to push the cell forward; thus, this model in theory explains how mechanical forces could drive cell migration (9, 10). However, other research presents conflicting data (11), likely due to the use of different experimental systems and cell tagging reagents. Moreover, most studies of individual cell motility use cultured cells or simple organisms, such that little is known about how membrane and vesicle motion coordinate to influence three-dimensional (3D) morphological changes of migrating cells in higher vertebrates.

In addition to the lipid portion of the plasma membrane that maintains fluidity of the cell boundary, the underlying cytoskeleton provides rigidity to the cell surface (12). A "treadmilling" model was used to explain cytoskeletal regulation of lamellipodial function (13, 14). According to this model, actin polymerization at the cell's leading edge and actin depolymerization at the back of the network (Fig. 1*B*) cause relative displacement to the cytosol, which subsequently "pulls" the rounded cell body. Yet, it is unclear whether and how actin turnover on the cell's basal side is coupled with other actin pools and membrane flow throughout the cells.

To address these long-standing cell biology questions in vivo, we directly visualize membrane and cytoskeletal behaviors in migrating neural crest cells at the trunk level of chicken embryos. The neural crest is one of the most migratory of embryonic cell types (15), initiating movement via an epithelial to mesenchymal transition from the neural tube (16). These multipotent cells then migrate throughout the periphery as individuals (17, 18), differentiating into diverse cells types including peripheral neurons, glia, and melanocytes of the skin (19). As neural crest-derived cells are prone to give rise to adult cancers, including melanoma, neuroblastoma, and gliomas, their innate migratory mode appears to be recapitulated during cancer metastasis (16). By combining live imaging with quantitative analysis, we extract dynamic molecular and cellular information about cell migration and utilize perturbation approaches to challenge it.

Results

As neural crest cells are a highly migratory cell type that navigates through a complex environment, they represent an ideal

Significance

Membrane and cytoskeletal dynamics are critical to cell motility. Extensively studied in cell culture, their roles in cell movement in vivo are less understood, especially in higher vertebrates. We use dynamic imaging to visualize membrane and cytoskeletal behavior in migrating neural crest cells in living tissue. We found that forward movement of individual neural crest cells is accompanied by circular membrane flow, from anterior-to-posterior apically and posterior-to-anterior basally, coupled with internalization of lipid vesicles via macropinocytosis in the soma. Macropinosomes become wrapped with actin, then undergo anterograde translocation via microtubules toward the lamellipodium, resulting in its expansion. We elucidate how actin dynamics and membrane flow are interacted to drive forward locomotion of individual cells.

Author contributions: Y.L. and W.G.G. designed research; Y.L., W.T., and S.G. performed research; Y.L., W.G.G., and A.A. contributed new reagents/analytic tools; Y.L., W.G.G., A.A., A.C., D.P., and C.L. analyzed data; and Y.L., W.G.G., and M.E.B. wrote the paper.

Reviewers: A.N., Instituto de Neurociencias de Alicante, Consejo Superior de Investigaciones Científicas–Universidad Miguel Hernández; and T.P., Stowers Institute for Medical Research.

Competing interest statement: M.E.B. and A.N. are listed as coauthors on a 2020 Consensus Statement. They did not collaborate directly on the paper.

This open access article is distributed under Creative Commons Attribution-NonCommercial-NoDerivatives License 4.0 (CC BY-NC-ND).

[1]To whom correspondence may be addressed. Email: mbronner@caltech.edu.

This article contains supporting information online at https://www.pnas.org/lookup/suppl/doi:10.1073/pnas.2007229117/-/DCSupplemental.

First published October 21, 2020.

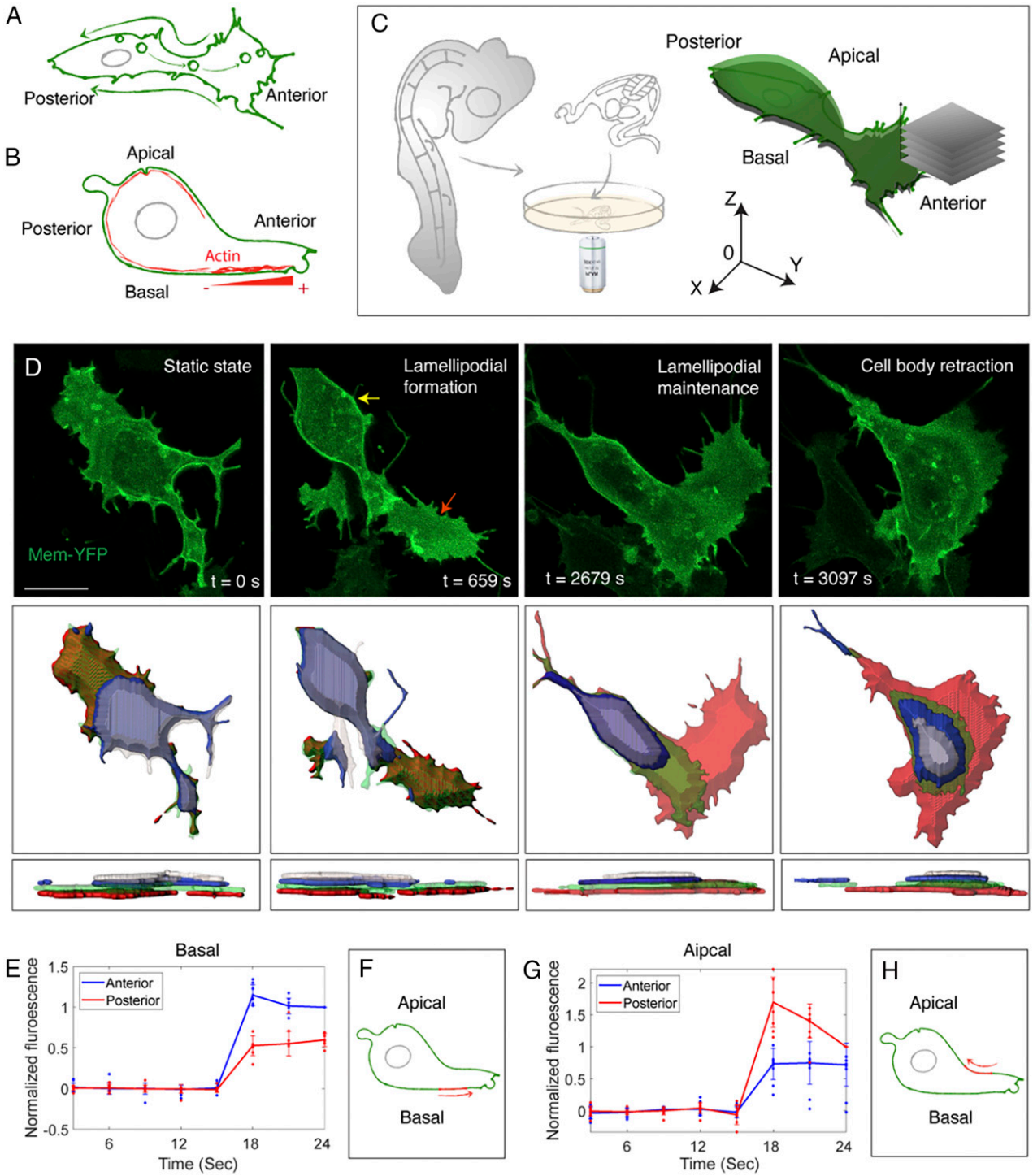

Fig. 1. Circular membrane flow across migrating cells. (*A*) The 2D "membrane flow" model from top view. Endocytosis at the posterior end produces vesicles that move toward the anterior end (arrows inside the cytoplasm); these vesicles integrate into the lamellipodium and then translate into retrograde membrane flow (arrows outside the cell). (*B*) The 3D "treadmilling" model from lateral view. F-actin (red) is distributed underneath the plasma membrane. In the basal side of the lamellipodium, actin displays a net polymerization toward the cell's anterior end. "−" and "+" represents depolymerization and polymerization end of actin, respectively. (*C*) Schematic illustration of explant culture and imaging. An ∼500-μm-thick transverse slice is dissected through the trunk of virally labeled chicken embryos for confocal time-lapse imaging. Successive movies of individual migrating cells are collected at different positions from the apical to the basal sides of the cell. For quantitative analysis, a coordinate system is used in which 0 denotes the center of the cell body. (*D*) Live imaging reveals a stereotypical fashion of cell migration (*Top*). A cell protrudes the lamellipodium (red arrow) and then progressively retracts its body (yellow arrow) toward the anterior end. The cell surface is computationally segmented with each optical slice pseudocolored. The surface area of individual segmented slices is measured, and the results are presented in *SI Appendix*, Fig. S1 *C* and *D*. (*Middle*) Top view. (*Bottom*) Lateral view. (Scale bar: 5 μm.) (*E–H*) Quantification of membrane flow based on the photo-conversion experiment (see *SI Appendix*, Fig. S1 *E–G* for details). On the basal side, anterior intensity of the red fluorescence is higher following photo-conversion (t = 15 s) (rank sum test in frame 6, $P < 0.001$, $n = 7$ cells) (*E*), suggesting anterior membrane flow (Schematic, *F*). This scenario is reversed on the apical side (rank sum test in frame 6, $P < 0.001$, $n = 8$ cells) (*G* and *H*).

system to study the movement of single cells in an in vivo context. We take advantages of individual cell labeling and dynamic imaging of chicken embryos to visualize intracellular events during active cell migration.

Circular Membrane Flow Across Migrating Cells. Using retrovirally mediated cell labeling in living slices of avian embryos (Fig. 1*C*) (18, 20, 21), we imaged Farnesylated-YFP–expressing cells to capture membrane dynamics, with high spatial (lateral: 0.076 μm per pixel; axial: 1 μm per pixel) and temporal (22 s per frame) resolution (Fig. 1*D*, *SI Appendix*, Fig. S1*A*, and Movie S1). We found that individual trunk neural crest cells in vivo migrate similarly to many other cell types including fibroblasts in vitro; first, there is extension of the lamellipodium, followed by retraction of the cell body. Consistent with this, similar cell morphology was observed in frozen tissue sections (*SI Appendix*, Fig. S1*B*). As a simple way to test for membrane recycling, we examined changes in cell volume. Although we observed remarkable changes in the surface area at different apicobasal layers, these changes occurred in opposite directions and thus canceled out (*SI Appendix*, Fig. S1 *C* and *D*). As a result, the average individual surface area and the total volume (sum of the surface area) of the neural crest cells remained relatively constant over the time of visualization (*SI Appendix*, Fig. S1 *C* and *D*), in line with the possibility of membrane recycling.

To directly assess membrane motion, we conducted a photoconversion assay on cells expressing Farnesylated-Dendra2, a protein that irreversibly turns from green to red fluorescence after 405-nm laser excitation (22). This approach highlights a small portion of the cell membrane for estimating the velocity of membrane flow. Illumination of a small region on the basal surface of the cell revealed membrane flow toward the anterior end (Fig. 1 *E* and *F*, *SI Appendix*, Fig. S1 *E* and *F*, and Movie S2). Conversely, the same experiment focusing on the apical side of the cells revealed posterior membrane movement (Fig. 1 *G* and *H*, *SI Appendix*, Fig. S1*G*, and Movie S2). These results contrast with the conventional model assuming retrograde membrane motion on both sides (7). Instead, it suggests circular membrane motion in a fashion that the membrane moves toward the anterior on the basal side and toward the posterior of the cell on the apical side.

Anterograde Flow of Type I Vesicles Expands the Lamellipodium. While the above scenario explains the maintenance of membrane integrity, it raises the question of how migrating cells attain polarity with more membrane material in the anterior for lamellipodial expansion (7). Answering this question requires determining the mobility of lipid vesicles in the cytoplasm (Fig. 2*A* and Movie S3). We noted that vesicle size appeared to correlate with their position and speed (*SI Appendix*, Fig. S1 *H–K*): Large vesicles (diameter more than 1.0 μm) were located on the apical side and exhibited slow movement; however, fast-moving small vesicles (diameter between 0.5 and 1.0 μm) were in distinct layers along the apical-basal axis. The relatively static state of large vesicles was inconsistent with a direct role in controlling lipid flow. Therefore, we focused on small vesicles and partitioned them into two classes depending on their site of origin: type I derived from the apical side of the cell body and type II derived from the lamellipodium (Fig. 2 *B* and *C*).

We first explored the kinetic behaviors of type I vesicles based on a coordinate system defined according to the cell's geometry (Fig. 1*C*). In the imaging plane, the anterior-posterior (major) axis of the cell was defined as the *y* axis with the *x* axis perpendicular to it. The *z* axis runs along the apical-basal axis (orthogonal to the image plane) of the cell. Decomposition of vesicle trajectories revealed that the vesicles fell into two clusters with distinct kinetics in the anterior-posterior direction (Fig. 2 *D* and *E*): 45% of the vesicles migrated long distance toward the basal/anterior end, whereas 55% moved within the cells body (Fig. 2 *F* and *G*). Along the *z* axis, vesicles were generally displaced in an apical to basal direction (Fig. 2*F*).

What are the consequences of the distinct migration trajectories of these two subgroups of type I vesicles on cell shape changes? We addressed this question using a custom software tool to quantify the relationship between the final destinations of vesicles and the protrusion of local cell membrane. Here, we followed the trajectories of individual vesicles; upon their fusion with the cell membrane, we calculated the change in the size of the local membrane (based on the intensity of Membrane-YFP) as a function of distance from the site of vesicle fusion. In this way, we found that vesicles moving into the front end fused with the membrane and expanded the lamellipodium (Fig. 2 *H–M*); however, those vesicles restricted to the cell body did not affect local cell morphology upon integrating into the membrane (Fig. 2 *N–S*).

As vesicle trajectories correlate with their contribution to cell morphogenesis, we next asked how vesicle motility is controlled (23). Conceptually, vesicle motion might reflect their bound versus unbound state to the cytoskeleton (24). Alternatively, these vesicles may always be bound to the cytoskeleton that, in turn, impacts vesicle dynamics. Visualizing the interaction between vesicles and cytoskeletal components in space and time offers a direct means to test between these two possibilities. To that end, we imaged distinct layers in the cells expressing Utrophin-scarlet, which binds to F-actin. The results showed a stereotypical distribution of F-actin subgroups with actin bundles on the basal region versus actin patches and cortical actin on the more apical side (*SI Appendix*, Fig. S2*A*) (25). While actin bundles are commonly used as tracks for endocytic transportation (26), their basal localization in neural crest cells cannot account for the apical-basal movement of type I vesicles.

Microtubules Mediate Anterograde Flow of Type I Vesicles. We subsequently assessed the spatial organization of microtubule (MT) using 2G4-GFP, an intrabody that specifically and noninvasively targets tubulin (27, 28). This labeling revealed a cable-like MT network, extending from the microtubule organizing center at the cell's apical/posterior region to the basal/anterior end (*SI Appendix*, Fig. S2*B*). Time-lapse imaging and colocalization analysis between MTs and vesicles further suggested that lipid migration occurred along this network (Fig. 3 *A* and *B* and Movie S4). Notably, we also observed vesicle motion on many MTs that filled the entire cell body (Movie S5). However, these vesicles moved more slowly than those associated with the lamellipodium (Fig. 3*C*). Such a patterned relationship between vesicle mobility and MT morphology supports the possibility that vesicles are in a bound state and their trajectories are substantially influenced by MT morphology.

Since the morphology of MTs is controlled by their growth orientation in many tissue systems (29), we tracked the MT plus end binding protein EB3 in neural crest cells to determine whether there is a correlation between MT dynamics and vesicle mobility (Fig. 3*D* and Movie S6). Following an established protocol (30), we measured the orientation of EB3 signal with respect to position in the cell (Fig. 3 *E–G*). As predicted, MTs showed less directional flow in the cell body than in the lamellipodium (Fig. 3 *H–J*). This helps to explain the differential mobility of the two subpopulations of type I vesicles. Based on these findings, we propose that MTs mediate anterograde flow of type I vesicles; this, in turn, integrates with circular membrane flow to create an endocytic cycle.

Type I Vesicles Are Noncanonical Macropinosomes Transporting F-Actin into the Lamellipodium. Given the stereotypical mobility of type I vesicles and their contributions to the cell's morphological changes, we next explored their nature. Clathrin-mediated endocytotic vesicles are typically of diameters smaller than 0.2 μm (31),

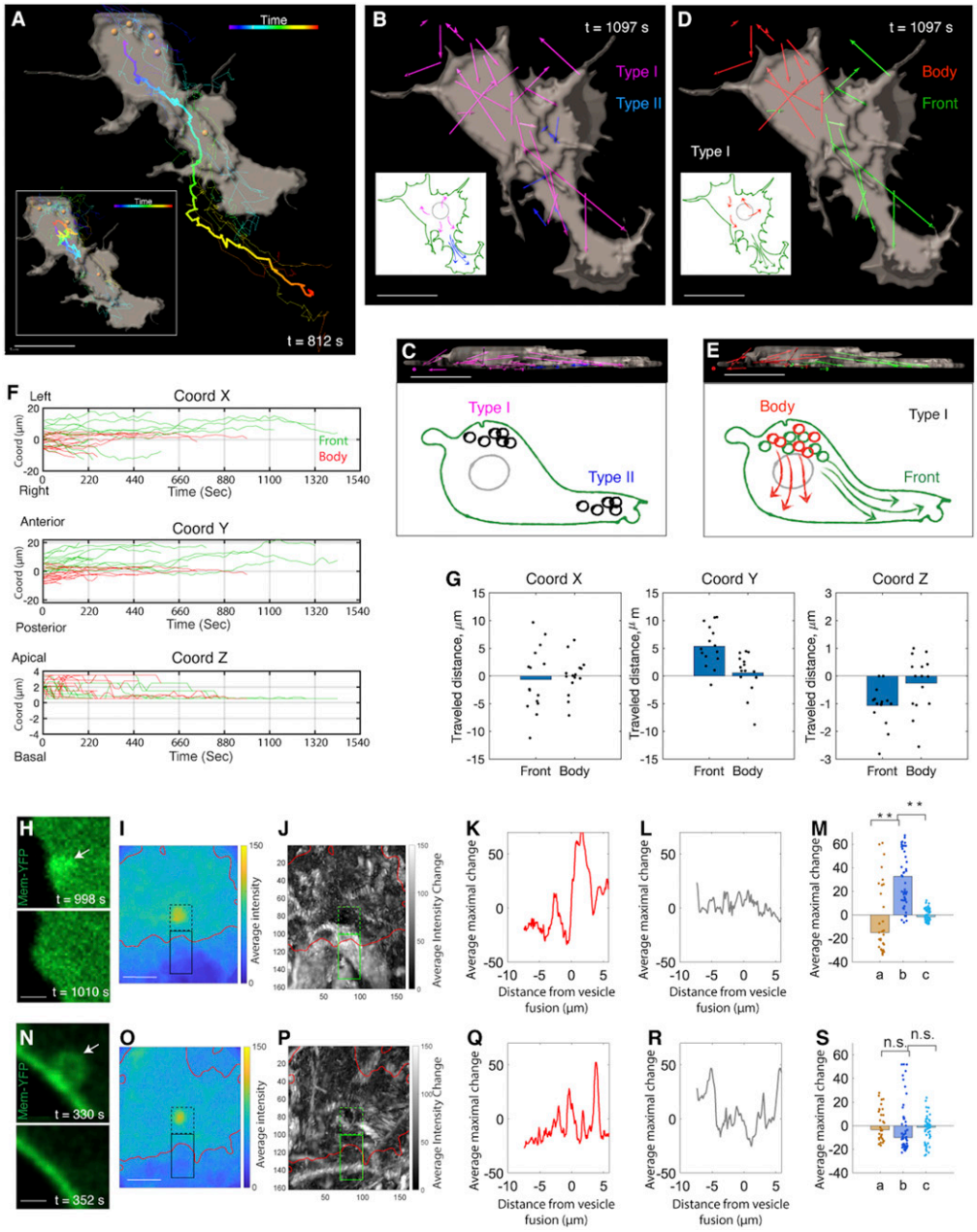

Fig. 2. Anterograde flow of type I vesicles expands the lamellipodium. (*A*) A segmented view of a migrating cell with its trajectory color-coded according to time (thick line). All of the vesicles inside the cell are segmented (yellow dots), and their trajectories are mapped (thin lines). (*Inset*) Vesicle motion is normalized relative to the movement of the center of the cell body. (Scale bar: 5 μm.) (*B* and *C*) Two types of vesicles from top (*B*) and lateral (*C*) view. The lengths of the net displacement vectors of type I and II vesicles are proportional to their moving distance inside the cell. The schematics illustrate vesicle trajectories. (Scale bars: 5 μm.) (*D* and *E*) Two subpopulations of type I vesicles from top (*D*) and lateral (*E*) view. Their net displacement vectors are presented with the ones moving to the front and the other moving inside the cell body. (Scale bars: 5 μm.) (*F*) Trajectory analysis of type I vesicles based on the coordinate system in Fig. 1*C*. The trajectories are color-coded according to their destinations along the anterior-posterior axis (*y* axis) ($n = 15$ and 18 for green and red, respectively). Green tracks show upward shift in this direction, meaning that these vesicles move toward the cell's front end. Along the *x* axis, upward shift of many green lines reflects lamellipodial extension toward the cell's left side. $n = 3$ cells. (*G*) Distance analysis confirms that the vesicles moving to the cell front show maximal displacement (along the *y* axis). $n = 15$ and 18 for vesicles moving to the front and in the cell body, respectively. $n = 3$ cells (rank sum test, *x*: $P = 0.724$; *y* = 0.001; *z*: $P = 0.018$). (*H–M*) Vesicles moving to the cell front expand the lamellipodium. (*H*) Two representative time frames showing vesicle (arrow) fusion into the membrane causes membrane protrusion. (*I–M*) Quantification (*Methods*). (*I*) The average intensity near the vesicle before fusion. The red contour shows the approximate cell membrane. The dashed and solid black contours show fluorescent signal inside and outside of the cells, respectively. (*J*) Average intensity change due to vesicle fusion. (*K–M*) The average maximum intensity changes as a function of distance from the site of vesicle fusion. Signal intensity decreases in the intracellular regions while increases in the extracellular regions (*K*); this is not observed in the random dataset (*L*). (*M*) Summary of the results in *K* and *L* (a: intracellular changes, b: extracellular changes, c: extracellular changes in the random dataset) (rank sum test, $^{**}P < 0.001$, $n = 31$ pixels representing the average across 36 vesicles). (*N–S*) Vesicle motion in the cell body does not impact cell morphology. (*N*) Two representative time frames. The same analysis in *I–M* is applied here. Note that the extracellular changes of the membrane (b) in *S* is not significantly different to intracellular changes (a) and the random dataset (c). $n = 3$ cells (rank sum test, $n = 31$ pixels representing the average across 36 vesicles). n.s., not significant. (Scale bars for *H*, *I*, *N*, *O*: 1 μm.)

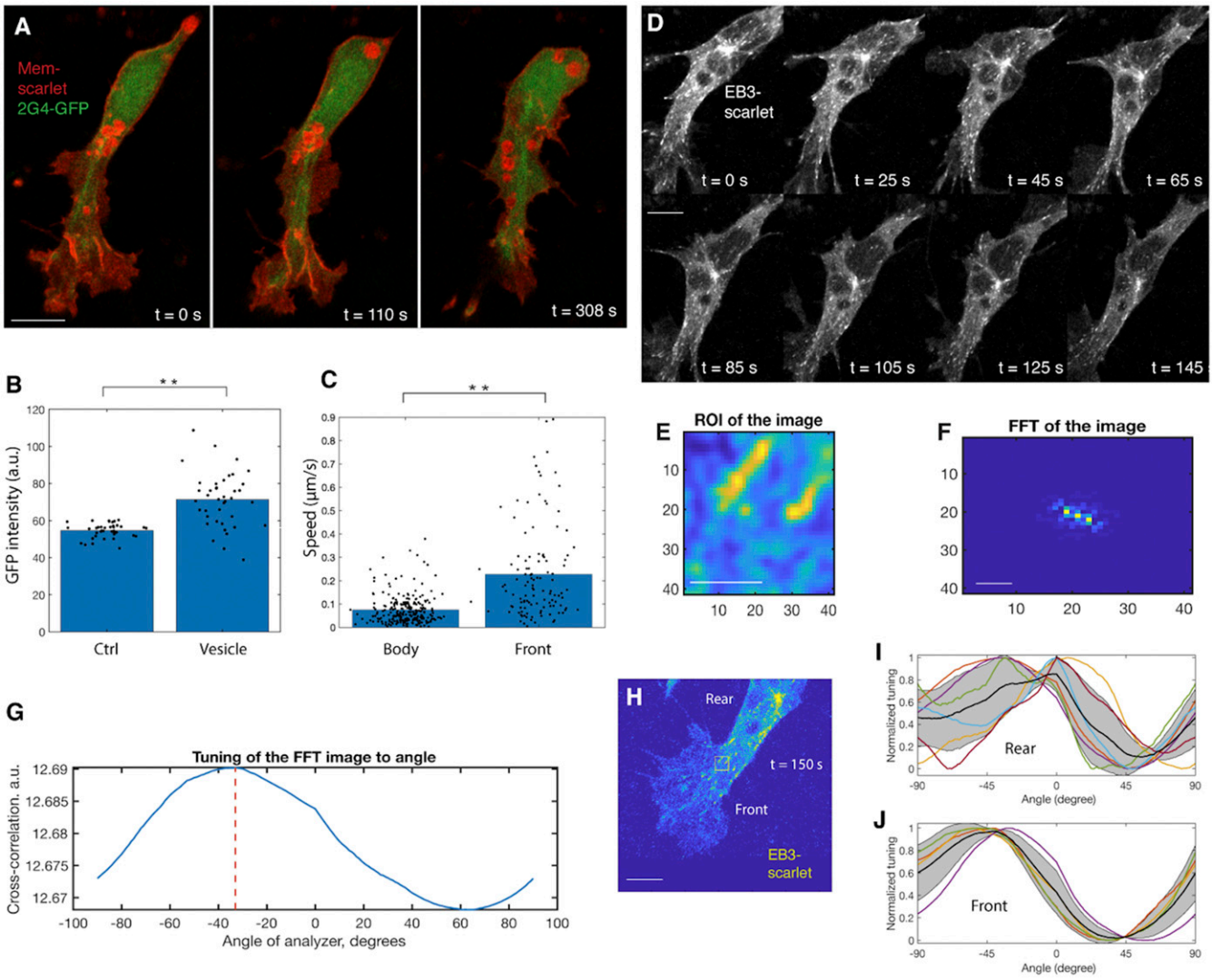

Fig. 3. MTs mediate anterograde flow of type I vesicles. (*A* and *B*) Live imaging of vesicle movement along MTs (*A*). (*B*) Fluorescence colocalization analysis shows that MT amount (2G4-GFP intensity) is higher in the region enriched with vesicles (Membrane-YFP intensity) compared with in the region without vesicles (Ctrl) (rank sum test, $^{**}P < 0.001$, $n = 3$ cells). (*C*) Speed analysis shows that vesicles in the lamellipodium move faster (rank sum test, $^{**}P < 0.001$, $n = 3$ cells). (*D*) Higher-frequency (collecting a frame every 5 s) imaging of MT plus ends. (Scale bar: 4 μm.) (*E*–*G*) Approach to measuring the orientation of MT plus ends (*Methods*). (*E*) In the region of interest (ROI), individual EB3 signal in *D* is zoomed in such that its shape can be clearly visualized. (*F*) For individual EB3 signal, its 2D fast Fourier transform (FFT) representation is calculated. (*G*) The cross-correlation between the orientation of FFT image and the long axis of cells is measured. This cross-correlation value represents the relative orientation of EB3 with respect to the cell. (*H*–*J*) Distinct flow orientation of MTs in the lamellipodium and in the cell body. In a randomly selected time frame (*H*), the approach introduced in *E*–*G* is applied to measure the orientation of EB3 flow. In *I* and *J*, bold black lines are the mean cross-correlation value for all EB3 signal. Gray area signifies SD, which positively correlates with the orientation of EB3. The higher SD in the cell body (*I*) than in the cell front (*J*) suggests that EB3 flow in the cell front end is more oriented. (Scale bar in *H*: 1 μm.)

whereas type I vesicles are much larger, having diameters of 0.5–1 μm (*SI Appendix*, Fig. S1*H*). Thus, these vesicles are unlikely to be clathrin-coated vesicles. Instead, they could either be the products of phagocytosis (e.g., by ingesting dead cells) or macropinocytosis (by absorbing fluids) (32). In a long term (up to 15 h) imaging session with a field of view covering more than 20 cells, only 1 cell was observed to engulf debris from dead cells (Fig. 4*A* and Movie S7); this is insufficient to account for the prevalence of type I vesicles in all observed cells. Meanwhile, several findings supported a possible role for macropinocytosis. This endocytic event is receptor independent but exhibits features of membrane ruffling, such as planar folding or circular extension which then engulfs liquid (33). Indeed, on the apical side of the cell body, we observed protrusion of the cell membrane into a cup-shaped structure that closed upon itself; in the subsequent retraction phase, the closed cup broke down into small vesicles (Fig. 4*B* and Movie S8). To further determine if these vesicles are in bona fide macropinosomes, we incubated the embryo slices with dextran, a commonly used vital dye to characterize macropinosome-mediated endocytosis (34), and observed immediate labeling of the vesicles (*SI Appendix*, Fig. S3*A* and Movie S9).

An independent assay for macropinocytosis is provided by inspecting the expression pattern of actin. During macropinocytosis, F-actin forms a belt-shaped band that surrounds the vesicles to generate contractile forces for vesicle fission, and this actin ring disappears when vesicles move into the cell (33). Analogously, we observed that cortical actin in neural crest cells initially binds to the plasma membrane in the cell body, ruptures as membrane protrusion retracts, and then associates with the cup-shaped membrane structure (Fig. 4*C* and Movie S10).

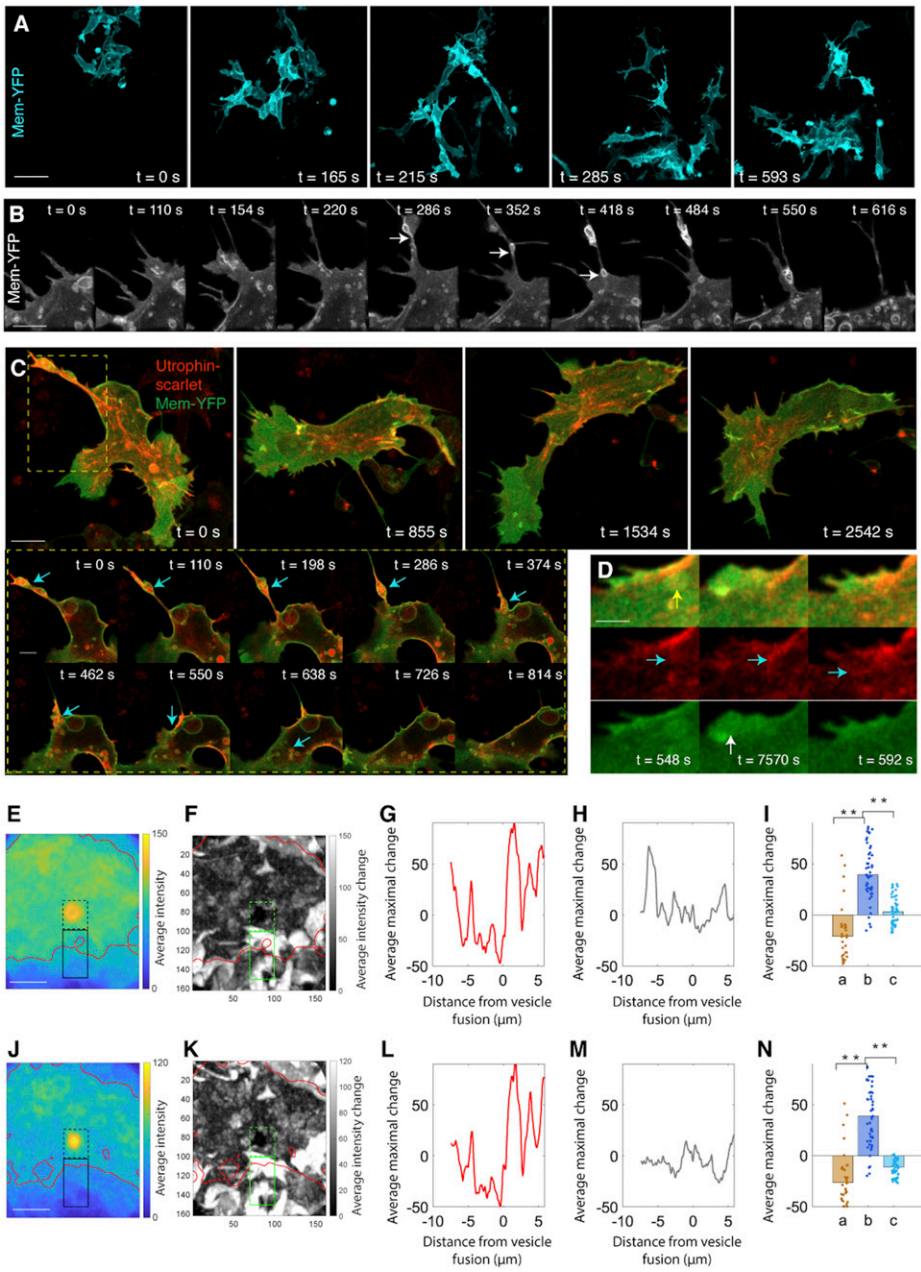

Fig. 4. Type I vesicles are noncanonical macropinosomes transporting F-actin to the lamellipodium. (*A*) Live imaging in a 612 × 612 × 13 μm^3 region between the dorsal neural tube and the notochord fails to detect evidence of phagocytosis. (Scale bar: 20 μm.) (*B*) Live imaging of macropinocytosis. The extending protrusion in the cell body retracts and translates into vesicles (arrows). (Scale bar: 3 μm.) (*C*) Live imaging on macropinosome wrapping of F-actin and subsequent transportation. (Scale bar: 4 μm). Box: zoom in view of the process of cortical actin breakage into actin patches, association with lipid vesicles and transportation into the lamellipodium (arrows) (Scale bar: 2 μm). (*D*) Addition of a F-actin patch into the actin bundles in the lamellipodium (green: Membrane-YFP; red: Utrophin-scarlet). When a vesicle moves to cell front (yellow arrow), its lipid causes membrane protrusion (white arrow); simultaneously, the actin patch inside this vesicle is released (cyan arrows) and merged with the existing actin bundles. (Scale bar: 1 μm.) (*E–N*) Morphological analysis confirms lipid expansion of cell membrane (*E–I*) and F-actin insertion into the lamellipodium (*J–N*). The same approach in Fig. 2 *I–M* is applied to assess the contribution of lipid and F-actin to lamellipodial morphogenesis. Focusing on *I*, increase of Membrane-YFP intensity in the extracellular region (b) suggests that lipid fusion causes membrane protrusion. Similarly, in *N*, increase of Utrophin-scarlet intensity in the extracellular region is a sign of F-actin insertion into the lamellipodium (for *I* and *N*, rank sum test, $^{**}P < 0.001$, $n = 31$ pixels representing the average of 17 vesicles). (Scale bars in *E* and *J*: 4 μm.)

Strikingly, instead of being gradually dissociated from the vesicles, F-actin further aggregated into small patches residing in the vesicles and moved together with the vesicles to the basal/anterior end (Fig. 4*C*, *SI Appendix*, Fig. S3*B*, and Movie S10). Using phalloidin staining, we confirmed that endogenous F-actin was wrapped by lipid vesicles (*SI Appendix*, Fig. S3*C*). Upon arriving in the lamellipodium, as the lipid components of the vesicles fused to the membrane, F-actin patches were docked into the actin module (Fig. 4 *D–N* and Movie S11).

We further characterized the relationship between these vesicles and actin, and found that F-actin inside the vesicles was more stable than that outside (*SI Appendix*, Fig. S3 *D* and *G* and Movie S12). In contrast, Actin-scarlet, labeling both F-actin and G-actin (actin monomer), was expressed at a lower level inside

the vesicles (*SI Appendix*, Fig. S3 *E* and *G* and Movie S12). In a control experiment, membrane bound Cortactin-scarlet showed similar expression patterns to total actin (*SI Appendix*, Fig. S3 *F* and *G* and Movie S12) (35). Collectively, this strongly suggests that the vesicles are comprised of low amounts of total actin with the majority being F-actin and operate as affinity and non-permeable transporters of F-actin. Hence, cortical actin in the cell body can transform into actin bundles in the lamellipodium through vesicular transportation (*SI Appendix*, Fig. S3*H*). Since these vesicles are distinct from classic macropinosomes with only transient actin interactions, we termed them noncanonical macropinosomes (Fig. 5*H*).

Type II Vesicles Are Canonical Macropinosomes Acting Inside the Lamellipodium. Next, we examined anteriorly located type II vesicles (Fig. 2 *B* and *C*) and demonstrated that they are canonical macropinosomes. In neural crest cells, some region of the lamellipodium folded into the apical side of the cell, further invaginated into the basal side and broke down into vesicles (Fig. 5 *A* and *B*). This phenomenon resembles planar folding of the plasma membrane during macropynocytosis (32). Unlike type I vesicles, these vesicles transiently bind to actin rings during their formation (Fig. 5*A* and Movie S13), a common feature of classic macropinosomes (33); afterward, they behave similarly to type I vesicles by moving along the MTs and expanding the plasma membrane (Fig. 5 *C*–*G*). These canonical macropinosomes may permit neural crest cells to quickly adjust the shape and size of the lamellipodium, thus operating as local control to complement to the global-scale influence of noncanonical macropinosomes (Fig. 5*H*).

Membrane Flow and Vesicle Flow Play Distinct Roles in Shaping the Lamellipodium. After determining the orientation of membrane motion and vesicle motion and their relationship, we segregated their contributions to cell morphogenesis. Given that MTs operate as the tracks for vesicle transportation (Fig. 3), they provide a valuable tool to manipulate vesicle mobility. Importantly, MT dynamics did not appear to impact membrane flow. In support of this, we analyzed the movements of membrane, MTs, and vesicles in the direction of cell migration (Fig. 6 *A* and *B* and *SI Appendix*, Fig. S4 *A* and *B*) and demonstrated these three processes occurred in a sequential order. This phenomenon further implies that membrane flow and vesicle flow are distinct and additive in defining the shape of the lamellipodium.

We functionally tested this possibility by blocking MT polymerization with nocodazole (29). Using a photo-conversion assay, we confirmed that nocodazole did not affect normal circulation of the plasma membrane (Fig. 6 *C* and *D* and Movie S14); hence, MTs do not directly control membrane mobility. However, several studies based on dynamic imaging (Fig. 6*E*) demonstrated a critical role for MTs in directing vesicle motion. In the treated cells, vesicles underwent fission (Fig. 6*F* and Movie S15) and moved more slowly than normal (*SI Appendix*, Fig. S4*D*). Consistent with this, vesicles' travel distance within the cells was shorter than normal (Fig. 6*H*) and these vesicles did not migrate close to the cell boundary (Fig. 6*G* and Movie S16) to integrate into the membrane. Although many treated cells extended long processes, these processes did not grow into a fan-shaped lamellipodium (Fig. 6*E* and Movie S1); instead, they receded into the cells, and repeated extension/retraction in the adjacent region (Fig. 6 *E* and *I* and Movie S17), a phenomenon referred to as cell blebbing (36). As expected, the aberrant vesicle kinetics and low F-actin composition (Fig. 6*I*) resulted in unsustainable growth of the bulging region (*SI Appendix*, Fig. S4*O*).

In many cell types, directional endocytic trafficking along MTs is regulated by Rab11, a small GTPase mediating the interactions between vesicles and other components including motor proteins, coat proteins, and scaffolding proteins (37). In neural crest cells, Rab11 colocalized with vesicles in neural crest cells (Fig. 7 *A*–*C*). Further, cells overexpressing a dominant-negative mutant form (DN-Rab11) exhibited normal features of MT organization (Fig. 7*D*), affording an additional experimental system to assess the influence of vesicle flow on cell morphogenesis. Within these cells, vesicles moved at normal speed (*SI Appendix*, Fig. S4*D*) but their migration was not as directional as the front-moving vesicles in the normal cells (Fig. 7 *E* and *F*, *SI Appendix*, Fig. S4*C*, and Movie S18). This was exemplified by the zigzag shapes of vesicle trajectories (*SI Appendix*, Fig. S4*F*) and their shorter moving distance (Fig. 7*H*). Compared with the nocodazole-treated cells, the phenotype of vesicle mobility in this scenario was more moderate and led to relatively small differences in both vesicle destinations and cell morphology. Due to their normal migration speed, these vesicles still moved to the cell boundary (Fig. 7*G*) and promoted membrane protrusion into the lamellipodium (*SI Appendix*, Fig. S4 *G*–*K*). Nevertheless, this event occurred in both cell anterior and posterior ends (Fig. 7 *E* and *G*), relating to the more random nature of vesicle trajectories (*SI Appendix*, Fig. S4*F*). Under these conditions, the lamellipodial structure was not maintained in one particular direction but retracted and then formed on the other side of the cells (Fig. 7*E* and *SI Appendix*, Fig. S4*O*), as validated by mapping angle progression of the lamellipodium (*SI Appendix*, Fig. S4 *L*–*N*).

Finally, since vesicles are generated through macropinocytosis, we asked whether this process also would be affected by nocodazole or DN-Rab11 treatment. We did not detect canonical macropinocytosis characterized by membrane folding in either case. Concomitantly, we noticed cup-shaped extensions of the noncanonical macropinocytosis and resultant vesicles in the cell body (Figs. 6*J* and 7*I*). Hence, upon interfering with normal vesicle mobility, canonical macropinocytosis is inhibited but noncanonical macropinocytosis still occurs, albeit producing vesicles with abnormal kinetics. As a consequence, cells exhibited unsustainable polarity (Figs. 6*E* and 7*E*) and impaired mobility (*SI Appendix*, Fig. S4*E*). Together, these results support the idea that membrane flow, vesicle fusion, and continuous vesicle flow, respectively, lead to membrane protrusion, lamellipodial formation, and lamellipodial maintenance.

Discussion

In this study, we identify a causal relationship between lipid and cytoskeleton to control cell migration in higher vertebrates. At the heart of our newly formulated model (Fig. 7*J*) lies the interaction between circular membrane motion and anterograde vesicle flow. Whereas the basal/anterior motion of the plasma membrane initiates lamellipodial formation, on the apical side, membrane flows toward the cell body and internalizes through noncanonical macropinocytosis. These vesicles transport F-actin along MTs to enhance the actin module and also shape the lamellipodium. Overlaid on this, canonical macropinocytosis regionally adjusts lamellipodial morphology. The whole intracellular recirculating system is driven by MT growth.

In contrast to the conventional "membrane-flow" model of bilateral retrograde flow of membrane, we present in vivo and 3D evidence to support anterograde flow of membrane at the cell's basal side and anterograde flow of vesicles inside the cytoplasm. We further show that these two flows sequentially extend the leading edge at the expense of membrane in the rear, and this results in a net forward displacement of the cell body. Such a scenario provides a physical linkage between membrane mobility and cell polarity, and may explain cell migration in the absence of traction force. To achieve the balance between cell shape change and lipid homeostasis, loss of lipid in in the rear is compensated for by the retrograde membrane flow on the apical side.

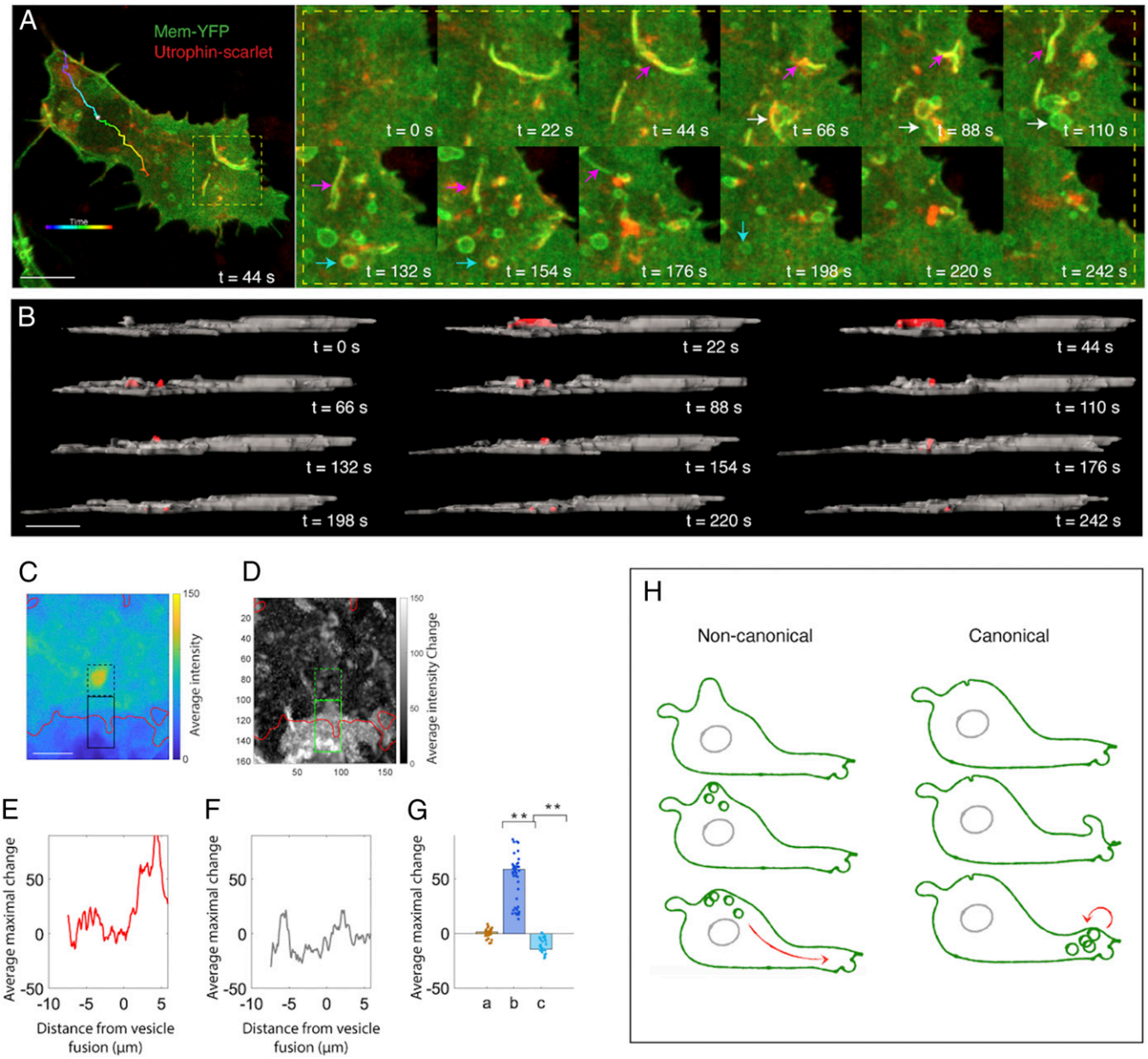

Fig. 5. Type II vesicles are canonical macropinosomes acting inside the lamellipodium. (*A*) Live imaging of the cellular process of type II macropinosytosis. The cell subjected to live imaging with its migratory trajectory (colored line). The box shows that within the lamellipodium membrane folding and degradation into vesicles; during this event, the vesicles only transiently bind to F-actin (arrows). The cyan arrows point to the actin rings (t = 132 s and t = 154 s). (*B*) A segmented and lateral view of the same cell presented in *A*. The folding part of the membrane and the resultant macropinosomes are labeled in red. (*C–G*) Lamellipodial extension by type II vesicles, as revealed by the same software tool in Fig. 2 *I–M*. Focusing on *G*, increase of Membrane-YFP intensity in the extracellular space (comparing b with a and c) demonstrates that lipid addition to the membrane results in cell protrusion (rank sum test, $P < 0.001$, $n = 31$ pixels representing the average of 22 vesicles). (Scale bars in *A–C*: 4 μm.) (*H*) Schematic representation of noncanonical macropinocytosis versus canonical macropinocytosis.

How is the membrane lipid translated into the cytoplasmic lipid? Based on the cell morphological analysis, dextran internalization assay and monitoring of actin behavior, our study highlights the importance of macropinocytosis throughout the cell for membrane internalization. We speculate that there are two advantages of macropinocytosis: (*i*) independence from specific receptors and (*ii*) the ability to exert both short-range and long-range effects on the lamellipodium through division of labor, providing cells with great flexibility to recycle lipids.

By analyzing actin evolution in neural crest cells in 3D embryos, we demonstrate that F-actin in the rear can directly fuel this actin pool through active shuttling. Our finding does not argue against "treadmilling" model (13, 14); rather it highlights multiple mechanisms in maintaining actin recirculation. As these F-actin patches are transported by the noncanonical macropinosomes, one possibility is that some actin-associated proteins incorporate into these vesicles during tail retraction; upon moving to the leading edge, both components (as an intact complex) thus could immediately participate in constructing the actin machinery. In turn, the organization of F-actin across the cells influences how vesicles sculpt cells at 3D level. Our data suggest that the periphery of the cell body is wrapped

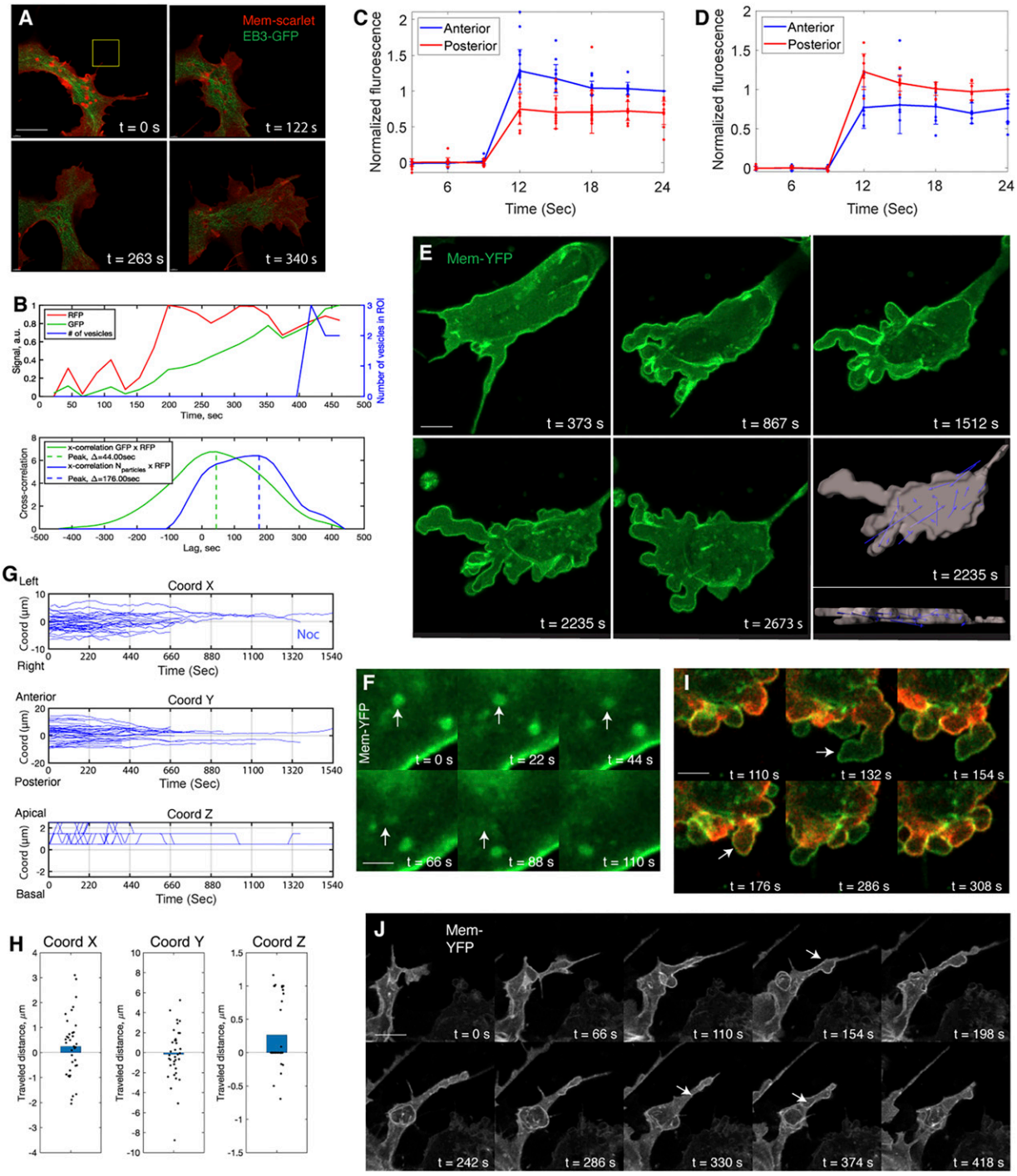

Fig. 6. Blocking MT polymerization interferes vesicle flow and lamellipodial formation. (*A* and *B*) Live imaging shows membrane protrusion occurs in advance of MT flow and vesicle flow (*A*). A window (yellow) is drawn in the direction of membrane extension, and the evolution of fluorescence signal of membrane, MT, and vesicles within this window is measured (*B*). *B, Upper* shows the sequential movements of the membrane, MT, and vesicles. (Scale bar in *A*: 4 μm.) (*C* and *D*) Normal membrane flow in the nocodazole-treated cells. The same photo-conversion assay to Fig. 1*E* is performed. (*C*) Photo-conversion on the basal side of the cells expressing Farnesylated-Dendra2 shows the red fluorescence move more quickly to the anterior end than to the posterior end (rank sum test at frame 4, $P < 0.001$, $n = 12$ cells). The same analysis on the apical side reveals posterograde membrane flow (rank sum test at frame 4, $P < 0.05$, $n = 7$ cells) (*D*). (*E*) Live imaging of a treated cell; note that the cell does not form the lamellipodium. In the segmented image, the displacement vectors are more randomized than the ones moving to the front in the normal cells in Fig. 2*D*. (Scale bar: 5 μm). (*F*) Live imaging to show vesicle fission (arrows) in the treated cells. (Scale bars: 2 μm.) (*G*) Trajectory analysis reveals abnormal vesicle movement in the treated cells. In both the medio-lateral (*x* axis) and anterior-posterior (*y* axis) directions, all of the lines extend toward 0 (the center of the cell body), demonstrating that vesicle motion is restricted within the cell body. (*H*) Distance analysis reveals minimal movement of the vesicles along the anterior-posterior axis of the treated cells (*y* axis), relative to their mobility in the normal cells in Fig. 2*G*, $n = 35$ vesicles, $n = 3$ cells (rank sum test, $P < 0.001$, *x*: $P = 0.241$; *y*: $P = 0.692$; *z*: $P = 0.004$). (*I*) The treated cells are blebbing. The expanding region is almost devoid of F-actin (t = 132 s, arrow); however, upon shrinkage, F-actin is enriched on the edge (t = 176 s, arrow) to exert contraction force. (Scale bar: 3 μm.) (*J*) Live imaging of noncanonical macropinocytosis in a treated cell. The ruffles on the cell body recede into the cytoplasm accompanied by vesicle delamination (arrows). The morphologies of these vesicles are not obvious due to fission. (Scale bar: 3 μm.)

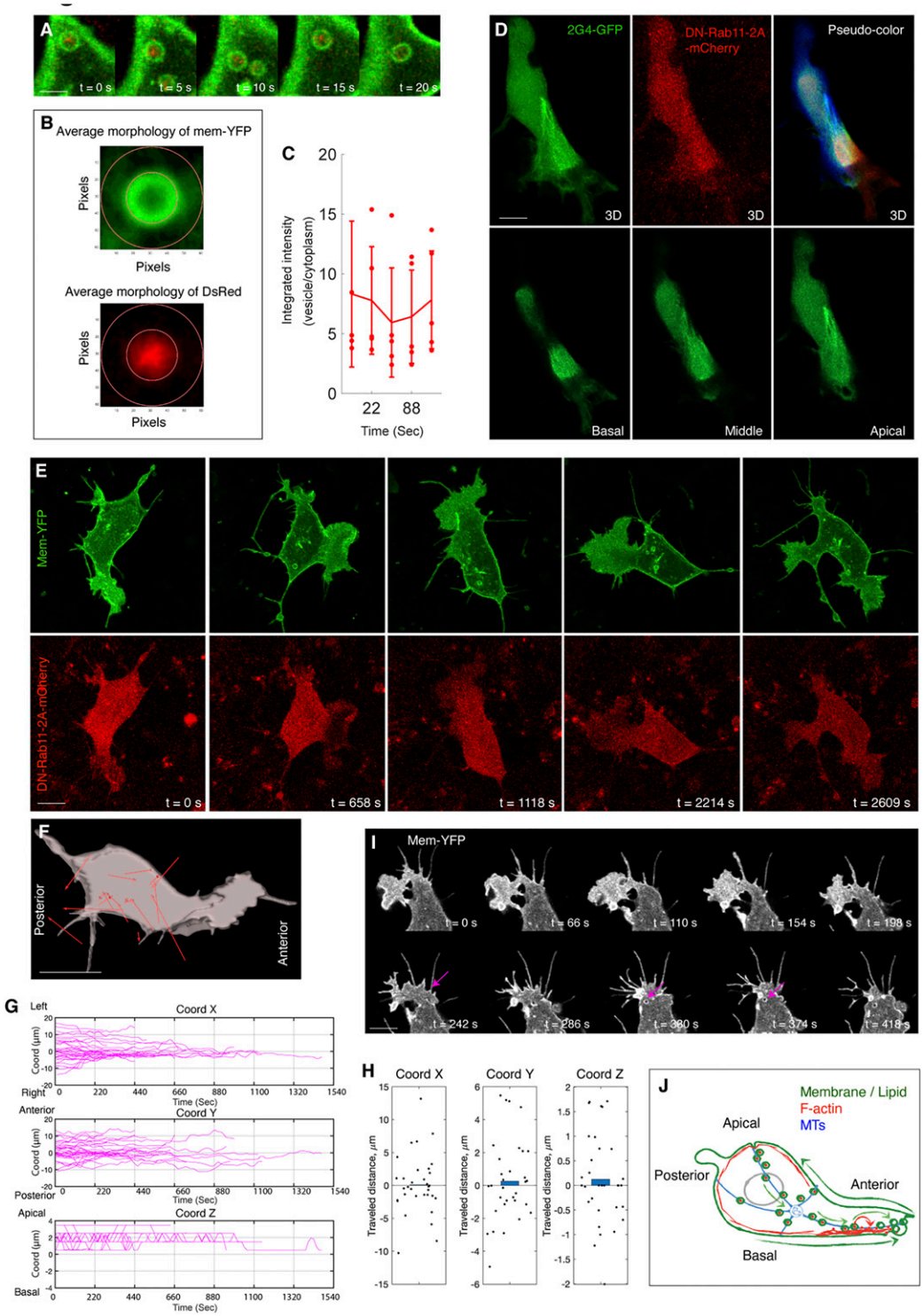

Fig. 7. Blocking Rab11 activity interferes vesicle flow and lamellipodial maintenance. (*A*–*C*) Rab11 is colocalized with vesicles. (*A*) Live imaging to show Rab11-DsRed labeled puncta (red) is enriched in the vesicles. *B* illustrates the principle of colocalization analysis. The inner ring is drawn along the border of Membrane-YFP (green). The red pixels in the inner ring and in the region between the inner and outside rings are measured. The ratio between them is plotted (*C*); if the ratio is more than one, it means more Rab11 inside the vesicles than in the cytoplasm. (Scale bar in *A*: 1 μm.) (*D*) MT organization in a DN-Rab11-2A-mCherry–positive cell. Three individual slices of the cell (from basal to apical side) are presented. In the 3D image (*Upper Right*), each individual slice is pseudocolored. Similar to the untreated cells in *SI Appendix*, Fig. S2*B*. (*E*) Live imaging of a DN-Rab11-2A-mCherry–expressing cell shows lamellipodial extension in multiple directions. (*F*) Net displacement vectors of the cell in *E* showing that vesicle movement is not directional. (Scale bars in *D*–*F*: 2 μm.) (*G*) Trajectory analysis of the vesicles in the DN-Rab11–positive cells. Along the *y* axis, the lines display both upward and downward shifts, the evidence of vesicle migration to either end of cells. $n = 35$ vesicles, $n = 3$ cells. (*H*) Distance analysis shows these vesicles move in shorter distance than the normal ones in Fig. 2*G*, $n = 35$ vesicles, $n = 3$ cells (rank sum test, $P < 0.001$, *x*: $P = 0.905$; *y*: $P = 0.543$; *z*: $P = 0.433$). (*I*) Live imaging of noncanonical macropinocytosis in a DN-Rab11–expressing cell. Similar to both untreated (Fig. 4*B*) and nocodazole treated cells (Fig. 6*J*), tail retraction produces small vesicles (arrows). (Scale bar: 3 μm.) (*J*) Schematic summary of the membrane and cytoskeletal processes in controlling cell polarization and locomotion.

by a layer of cortical actin, which functions like a physical fence to prevent cell protrusions after lipid addition. In contrast, the lamellipodium is free of cortical actin. This helps to explain why, despite the existence of vesicles fusion to the membrane in both the cell body and the lamellipodium, only the latter leads to morphological change.

Considering that regulation of transcription, translation, and ubiquitin-mediated protein degradation takes significant amounts of time that are likely too long to enable rapid morphological changes in migrating cells, recycling and redistributing of the existing cellular components appears to be a more direct means to solve this problem. Our study elucidates the recirculating system that unifies different cellular components, supporting the idea of "efficiency through simplicity." Identification of a linkage between membrane and cytoskeletal dynamics in neural crest cells provides a predictive model that can be tested for other motile cells including cancer cells. Advanced imaging techniques such as multiphoton imaging (38), fluorescence lifetime imaging (39), fluorescence spectroscopy microscopy (40), second harmonic generation (41), hyperspectral imaging (42), and light sheet imaging in the near-infrared II window (43) will provide solutions to this challenge.

Materials and Methods

Molecular Cloning and Viral Production. Recombinant RIA plasmids were cotransfected with Envelop A plasmid into chick DF1 cells in 15-cm culture dishes using standard transfection protocol (20). When the cells were confluent, the cell culture medium was harvested once per day for 3 d and was concentrated at 26,000 rpm for 1.5 h. The pellet was dissolved in a minimal volume of DMEM.

Viral Infection and Explant Culture of Chicken Embryos. Fertilized chicken eggs were incubated at 38 °C until embryos reached stages HH11+/12- (44). To achieve efficient transfection of the neural tube and neural crest cells, concentrated virus (10^6 to 10^7 pfu/mL) were injected into the posterior neuropore, filling the entire tube. Injected embryos were incubated at 38 °C for 24 h, collected with filter paper carriers, and washed in Ringer's solution. Transverse cuts through posterior sclerotomes of the forelimb region were made every two somites and put into fluorodish-containing Neurobasal media.

Image Acquisition and Segmentation. The whole fluorodish was transferred into the incubation chamber (37 °C and 5% CO_2) of a Zeiss LSM 800 inverted microscope for time-lapse imaging. For all imaging experiments, optical sectioning was achieved at 1-μm intervals. For long-term imaging of Faenesylated-YFP–expressing cells to detect phagocytosis, 20 ×/0.8 N.A. objective was used and digital amplification was set to 0.6. The samples were excited by 488-nm laser with 0.8% relative power and imaged at 2-min intervals for 12 h. For imaging MT and EB3 dynamics, 63×/1.4 N.A. objective lens was used and digital amplification was set to 3. The samples were imaged at 5-s intervals. 2G4-GFP and EB3-Sarlet were excited by 488-nm laser with 0.4% relative power and 561-nm laser with 0.7% relative power, relatively. The four-dimensional (4D) images were imported into IMARIS 9.3. Three-dimensional surface segmentation of cells, 3D spot segmentation, and 4D tracking of vesicles were performed.

Analysis of Lipid Addition to Cell Membrane. Corresponding to Fig. 2*H*, the last frame of every vesicle was identified. The field of view was rotated so that the membrane nearest the last observed position of the vesicle is oriented vertically downward (i). Thus, the last observed vesicle position is at the center and the nearest membrane is at the bottom. The average across all vesicles is shown in Fig. 2*I*. The inside of the cell is delineated by the solid red line marking average membrane intensities above 43 (arbitrary units). The resulting membrane extension due to vesicle fusion (J), calculated by the difference between last frame in which the vesicle was observed and the next frame. The green contour shows the largest changes in the membrane, which are mainly localized to the extracellular region (red contour).

Data Availability. All study data are included in the article and supporting information.

ACKNOWLEDGMENTS. We thank Pierre Martineau for sharing reagents and Beckman Institute Biological Imaging Facility at Caltech for sharing equipment. We thank the Beckman Institute at Caltech for financial support to the Center for Advanced Methods in Biological Image Analysis (A.C.). W.G.G. is supported by the Della Martin Foundation, the American Heart Association, and the Burroughs Wellcome Fund. S.G. is supported by the American Heart Association. This project is supported by DE024157 and R35NS111564 (to M.E.B.).

1. K. M. Yamada, M. Sixt, Mechanisms of 3D cell migration. *Nat. Rev. Mol. Cell Biol.* **20**, 738–752 (2019).
2. A. W. Lambert, D. R. Pattabiraman, R. A. Weinberg, Emerging biological principles of metastasis. *Cell* **168**, 670–691 (2017).
3. D. T. Burnette *et al*., A role for actin arcs in the leading-edge advance of migrating cells. *Nat. Cell Biol.* **13**, 371–381 (2011).
4. T. Mseka, L. P. Cramer, Actin depolymerization-based force retracts the cell rear in polarizing and migrating cells. *Curr. Biol.* **21**, 2085–2091 (2011).
5. R. B. Taylor, W. P. H. Duffus, M. C. Raff, S. de Petris, Redistribution and pinocytosis of lymphocyte surface immunoglobulin molecules induced by anti-immunoglobulin antibody. *Nat. New Biol.* **233**, 225–229 (1971).
6. M. S. Bretscher, Particle migration on cells. *Nature* **341**, 491–492 (1989).
7. M. S. Bretscher, Getting membrane flow and the cytoskeleton to cooperate in moving cells. *Cell* **87**, 601–606 (1996).
8. M. S. Bretscher, Asymmetry of single cells and where that leads. *Annu. Rev. Biochem.* **83**, 275–289 (2014).
9. P. R. O'Neill *et al*., Membrane flow drives an adhesion-independent amoeboid cell migration mode. *Dev. Cell* **46**, 9–22.e4 (2018).
10. M. Tanaka *et al*., Turnover and flow of the cell membrane for cell migration. *Sci. Rep.* **7**, 12970 (2017).
11. J. D. Howe, N. P. Barry, M. S. Bretscher, How do amoebae swim and crawl? *PLoS One* **8**, e74382 (2013).
12. C. Simon *et al*., Actin dynamics drive cell-like membrane deformation. *Nat. Phys.* **15**, 602–609 (2019).
13. T. D. Pollard, G. G. Borisy, Cellular motility driven by assembly and disassembly of actin filaments. *Cell* **112**, 453–465 (2003).
14. A. Ponti, M. Machacek, S. L. Gupton, C. M. Waterman-Storer, G. Danuser, Two distinct actin networks drive the protrusion of migrating cells. *Science* **305**, 1782–1786 (2004).
15. N. Le Douarin, *The Neural Crest* (Cambridge University Press, 1982).
16. J. P. Thiery, H. Acloque, R. Y. J. Huang, M. A. Nieto, Epithelial-mesenchymal transitions in development and disease. *Cell* **139**, 871–890 (2009).
17. A. Shellard, A. Szabó, X. Trepat, R. Mayor, Supracellular contraction at the rear of neural crest cell groups drives collective chemotaxis. *Science* **362**, 339–343 (2018).
18. Y. Li *et al*., In Vivo quantitative imaging provides insights into trunk neural crest migration. *Cell Rep.* **26**, 1489–1500.e3 (2019).
19. M. E. Bronner, M. Simões-Costa, The neural crest migrating into the twenty-first century. *Curr. Top. Dev. Biol.* **116**, 115–134 (2016).
20. Y. Li, A. Li, J. Junge, M. Bronner, Planar cell polarity signaling coordinates oriented cell division and cell rearrangement in clonally expanding growth plate cartilage. *eLife* **6**, e23279 (2017).
21. W. Tang, Y. Li, S. Gandhi, M. E. Bronner, Multiplex clonal analysis in the chick embryo using retrovirally-mediated combinatorial labeling. *Dev. Biol.* **450**, 1–8 (2019).
22. N. G. Gurskaya *et al*., Engineering of a monomeric green-to-red photoactivatable fluorescent protein induced by blue light. *Nat. Biotechnol.* **24**, 461–465 (2006).
23. C. P. Brangwynne, G. H. Koenderink, F. C. MacKintosh, D. A. Weitz, Intracellular transport by active diffusion. *Trends Cell Biol.* **19**, 423–427 (2009).
24. M. Kaksonen, Y. Sun, D. G. Drubin, A pathway for association of receptors, adaptors, and actin during endocytic internalization. *Cell* **115**, 475–487 (2003).
25. A. J. Ridley, Life at the leading edge. *Cell* **145**, 1012–1022 (2011).
26. M. Schuh, An actin-dependent mechanism for long-range vesicle transport. *Nat. Cell Biol.* **13**, 1431–1436 (2011).
27. L. Cassimeris, L. Guglielmi, V. Denis, C. Larroque, P. Martineau, Specific in vivo labeling of tyrosinated α-tubulin and measurement of microtubule dynamics using a GFP tagged, cytoplasmically expressed recombinant antibody. *PLoS One* **8**, e59812 (2013).
28. J. Zenker *et al*., Expanding actin rings zipper the mouse embryo for blastocyst formation. *Cell* **173**, 776–791.e17 (2018).
29. J. Zenker *et al*., A microtubule-organizing center directing intracellular transport in the early mouse embryo. *Science* **357**, 925–928 (2017).
30. Z. Q. Liu, Scale space approach to directional analysis of images. *Appl. Opt.* **30**, 1369–1373 (1991).
31. M. Kaksonen, C. P. Toret, D. G. Drubin, Harnessing actin dynamics for clathrin-mediated endocytosis. *Nat. Rev. Mol. Cell Biol.* **7**, 404–414 (2006).
32. J. A. Swanson, Shaping cups into phagosomes and macropinosomes. *Nat. Rev. Mol. Cell Biol.* **9**, 639–649 (2008).

33. J. Mercer, A. Helenius, Virus entry by macropinocytosis. *Nat. Cell Biol.* **11**, 510–520 (2009).
34. C. Chiasson-MacKenzie *et al*., Merlin/ERM proteins regulate growth factor-induced macropinocytosis and receptor recycling by organizing the plasma membrane:cytoskeleton interface. *Genes Dev.* **32**, 1201–1214 (2018).
35. N. Inagaki, H. Katsuno, Actin waves: Origin of cell polarization and migration? *Trends Cell Biol.* **27**, 515–526 (2017).
36. G. T. Charras, J. C. Yarrow, M. A. Horton, L. Mahadevan, T. J. Mitchison, Non-equilibration of hydrostatic pressure in blebbing cells. *Nature* **435**, 365–369 (2005).
37. E. Schonteich *et al*., The Rip11/Rab11-FIP5 and kinesin II complex regulates endocytic protein recycling. *J. Cell Sci.* **121**, 3824–3833 (2008).
38. Y. Li *et al*., Dynamic imaging of the growth plate cartilage reveals multiple contributors to skeletal morphogenesis. *Nat. Commun.* **6**, 6798 (2015).
39. Y. Li *et al*., Discs large 1 controls daughter-cell polarity after cytokinesis in vertebrate morphogenesis. *Proc. Natl. Acad. Sci. U.S.A.* **115**, E10859–E10868 (2018).
40. G. Kaur *et al*., Probing transcription factor diffusion dynamics in the living mammalian embryo with photoactivatable fluorescence correlation spectroscopy. *Nat. Commun.* **4**, 1637 (2013).
41. P. J. Campagnola, L. M. Loew, Second-harmonic imaging microscopy for visualizing biomolecular arrays in cells, tissues and organisms. *Nat. Biotechnol.* **21**, 1356–1360 (2003).
42. F. Cutrale *et al*., Hyperspectral phasor analysis enables multiplexed 5D in vivo imaging. *Nat. Methods* **14**, 149–152 (2017).
43. F. Wang *et al*., Light-sheet microscopy in the near-infrared II window. *Nat. Methods* **16**, 545–552 (2019).
44. V. Hamburger, H. L. Hamilton, A series of normal stages in the development of the chick embryo. *J. Morphol.* **88**, 49–92 (1951).